Article

Structural Insights into Nonheme Alkylperoxoiron(III) and Oxoiron(IV) Intermediates by X-ray Absorption Spectroscopy

Jan-Uwe Rohde, Stphane Torelli, Xiaopeng Shan, Mi Hee Lim, Eric J. Klinker, Jzsef Kaizer, Kui Chen, Wonwoo Nam, and Lawrence Que

J. Am. Chem. Soc., **2004**, 126 (51), 16750-16761• DOI: 10.1021/ja047667w • Publication Date (Web): 02 December 2004

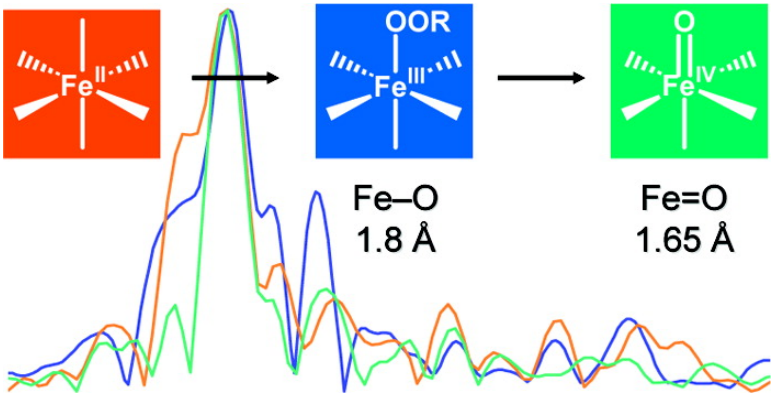

More About This Article

Additional resources and features associated with this article are available within the HTML version:

- Supporting Information
- Links to the 10 articles that cite this article, as of the time of this article download
- Access to high resolution figures
- Links to articles and content related to this article
- Copyright permission to reproduce figures and/or text from this article

View the Full Text HTML

J|A|C|S
ARTICLES
Published on Web 12/02/2004

Structural Insights into Nonheme Alkylperoxoiron(III) and Oxoiron(IV) Intermediates by X-ray Absorption Spectroscopy

Jan-Uwe Rohde,[†] Stéphane Torelli,[†] Xiaopeng Shan,[†] Mi Hee Lim,[†,‡] Eric J. Klinker,[†] József Kaizer,[†] Kui Chen,[†] Wonwoo Nam,[‡] and Lawrence Que, Jr.*[,†]

Department of Chemistry and Center for Metals in Biocatalysis, University of Minnesota, 207 Pleasant Street SE, Minneapolis, Minnesota 55455, and Department of Chemistry, Division of Nano Sciences, and Center for Biomimetic Systems, Ewha Womans University, Seoul 120-750, Korea

Received April 22, 2004; E-mail: que@chem.umn.edu

Abstract: Transient mononuclear low-spin alkylperoxoiron(III) and oxoiron(IV) complexes that are relevant to the activation of dioxygen by nonheme iron enzymes have been generated from synthetic iron(II) complexes of neutral tetradentate (TPA) and pentadentate (N4Py, Bn-TPEN) ligands and structurally characterized by means of Fe K-edge X-ray absorption spectroscopy (XAS). Notable features obtained from fits of the EXAFS region are Fe−O bond lengths of 1.78 Å for the alkylperoxoiron(III) intermediates and 1.65−1.68 Å for the oxoiron(IV) intermediates, reflecting different strengths in the Fe−O π interactions. These differences are also observed in the intensities of the 1s-to-3d transitions in the XANES region, which increase from 4 units for the nearly octahedral iron(II) precursor to 9−15 units for the alkylperoxoiron(III) intermediates to 25−29 units for the oxoiron(IV) species.

Introduction

Many mononuclear nonheme iron enzymes are involved in dioxygen metabolism. They activate dioxygen to carry out metabolically important oxidative transformations and are involved in the detoxification of superoxide. Their active sites have become well characterized through spectroscopic investigations and the solution of crystal structures for not only the as isolated resting state but also for binary, ternary, and quaternary complexes as well.[1−4] Catalytic mechanisms for these enzymes invariably invoke metal-peroxo and/or high-valent metal-oxo species during turnover. For example, peroxo intermediates have been observed in solution in the chemistry of the antitumor drug bleomycin,[5] superoxide reductase,[6−9] and lipoxygenase,[10] while an oxoiron(IV) intermediate has recently been identified in the catalytic cycle of the 2-oxoglutarate-dependent monoiron enzyme TauD.[11−13] Crystallographic information is available for two intermediates. A structure of the purple alkylperoxo intermediate of soybean lipoxygenase-3 derived from substrate oxidation revealed an end-on bound alkylperoxo ligand to the iron(III) center,[10] while a more recent report on naphthalene dioxygenase in complex with substrate and O_2 showed a side-on dioxygen moiety coordinated to the iron center.[14]

Model compounds can play an important role in establishing the structural descriptions of enzymic intermediates and contribute to our understanding of their spectroscopic and reactivity properties. With synthetic nonheme iron complexes, it has been possible to generate a number of peroxoiron(III) species stabilized at low temperature.[15,16] Since crystal structures for none of these are available, X-ray absorption spectroscopy (XAS) has become the experimental tool of choice to determine intramolecular distances and to gain insight into the metal environments of these intriguing intermediates. To date, this approach has been applied to $[Fe^{III}(S^{Me2}N_4(tren))(OOH)]^+$,[17,18] $[Fe^{III}(N4Py)(OOH)]^{2+}$,[19] $[Fe^{III}(N4Py)(\eta^2\text{-}O_2)]^+$,[19] and $[Fe^{III}(PaPy3)(OOH)]^+$ [20] and sheds some light on how the strength of the $Fe-O_{peroxo}$ bond is affected by differences in the

[†] University of Minnesota.
[‡] Ewha Womans University.

(1) Schofield, C. J.; Zhang, Z. *Curr. Opin. Struct. Biol.* **1999**, *9*, 722−731.
(2) Solomon, E. I.; Brunold, T. C.; Davis, M. I.; Kemsley, J. N.; Lee, S.-K.; Lehnert, N.; Neese, F.; Skulan, A. J.; Yang, Y.-S.; Zhou, J. *Chem. Rev.* **2000**, *100*, 235−349.
(3) Fitzpatrick, P. F. *Biochemistry* **2003**, *42*, 14083−14091.
(4) Costas, M.; Mehn, M. P.; Jensen, M. P.; Que, L., Jr. *Chem. Rev.* **2004**, *104*, 939−986.
(5) Burger, R. M. *Chem. Rev.* **1998**, *98*, 1153−1169.
(6) Coulter, E. D.; Emerson, J. P.; Kurtz, D. M., Jr.; Cabelli, D. E. *J. Am. Chem. Soc.* **2000**, *122*, 11555−11556.
(7) Emerson, J. P.; Coulter, E. D.; Cabelli, D. E.; Phillips, R. S.; Kurtz, D. M., Jr. *Biochemistry* **2002**, *41*, 4348−4357.
(8) Mathé, C.; Mattioli, T. A.; Horner, O.; Lombard, M.; Latour, J.-M.; Fontecave, M.; Nivière, V. *J. Am. Chem. Soc.* **2002**, *124*, 4966−4967.
(9) Nivière, V.; Asso, M.; Weill, C. O.; Lombard, M.; Guigliarelli, B.; Favaudon, V.; Houée-Levin, C. *Biochemistry* **2004**, *43*, 808−818.
(10) Skrzypczak-Jankun, E.; Bross, R. A.; Carroll, R. T.; Dunham, W. R.; Funk, M. O., Jr. *J. Am. Chem. Soc.* **2001**, *123*, 10814−10820.
(11) Price, J. C.; Barr, E. W.; Tirupati, B.; Bollinger, J. M., Jr.; Krebs, C. *Biochemistry* **2003**, *42*, 7497−7508.
(12) Price, J. C.; Barr, E. W.; Glass, T. E.; Krebs, C.; Bollinger, J. M., Jr. *J. Am. Chem. Soc.* **2003**, *125*, 13008−13009.
(13) Proshlyakov, D. A.; Henshaw, T. F.; Monterosso, G. R.; Ryle, M. J.; Hausinger, R. P. *J. Am. Chem. Soc.* **2004**, *126*, 1022−1023.
(14) Karlsson, A.; Parales, J. V.; Parales, R. E.; Gibson, D. T.; Eklund, H.; Ramaswamy, S. *Science* **2003**, *299*, 1039−1042.
(15) Girerd, J.-J.; Banse, F.; Simaan, A. J. *Struct. Bonding* **2000**, *97*, 145−177.
(16) Rohde, J.-U.; Bukowski, M. R.; Que, L., Jr. *Curr. Opin. Chem. Biol.* **2003**, *7*, 674−682.
(17) Shearer, J.; Scarrow, R. C.; Kovacs, J. A. *J. Am. Chem. Soc.* **2002**, *124*, 11709−11717.

10.1021/ja047667w CCC: $27.50

supporting ligand, the peroxo binding mode, and the metal spin state. In addition, computational methods have been useful for assessing likely structures and predicting the $Fe-O_{peroxo}$ bond length.[19,21−24]

In the area of high-valent oxoiron intermediates, we have recently reported the generation and isolation of the first examples of mononuclear nonheme oxoiron(IV) species from synthetic iron(II) precursors. Complexes with a terminal Fe^{IV}═O unit have now been obtained with TMC, TPA, N4Py, and Bn-TPEN as supporting ligands via reactions with stoichiometric peracid or iodosylbenzene as oxygen donors and extensively characterized by various spectroscopic techniques.[18,25−27] Only for the TMC complex has a high-resolution crystal structure been obtained to demonstrate unequivocally that a terminal Fe^{IV}═O unit can indeed exist in a nonporphyrin ligand environment.[25]

To augment the very limited amount of structural information available for metastable peroxoiron(III) and oxoiron(IV) intermediates, we have conducted a detailed X-ray absorption spectroscopic study of two low-spin $[Fe^{III}(L)(OO^tBu)]^{2+}$ (L = TPA, N4Py) and four low-spin $[Fe^{IV}(O)(L)]^{2+}$ complexes (L = TPA, N4Py, Bn-TPEN). The results reported in this paper represent the most extensive structural examination thus far of a related series of intermediates relevant to the catalytic cycles of mononuclear nonheme iron enzymes involved in dioxygen metabolism.

Experimental Section

Materials and General Procedures. All reagents and solvents were purchased from commercial sources and were used as received, unless noted otherwise. Solvents were dried according to published procedures and distilled under Ar prior to use.[28] Preparation and handling of air-sensitive materials were carried out under an inert atmosphere by using either standard Schlenk and vacuum line techniques or a glovebox. Elemental analyses were performed by Atlantic Microlab, Inc., Norcross, GA.

Preparation of Iron(II) Precursors. $[Fe(TPA)(NCMe)_2](ClO_4)_2$,[29] **1a**$(ClO_4)_2$, $[Fe(TPA)(OTf)_2]$,[26] $[Fe(N4Py)(NCMe)](ClO_4)_2$,[30] **1b**$(ClO_4)_2$, and [Fe(Bn-TPEN)(OTf)](OTf),[27] **1c**(OTf), were synthesized according to published procedures. ***Caution:*** perchlorate salts of metal complexes with organic ligands are potentially explosive and should be handled with care! The preparation of $[^{57}Fe(TPA)(OTf)_2]$ was carried out analogously to the natural abundance compound using $^{57}Fe(OTf)_2$·2 MeCN. $[^{57}Fe(N4Py)(NCMe)](ClO_4)_2$ was prepared as described previously.[30]

$[Fe(N4Py)(NCMe)](OTf)_2$, 1b$(OTf)_2$. 290 mg (0.38 mmol) N4Py·4 $HClO_4$[31,32] were dissolved in 10 mL distilled H_2O and 10 mL CH_2Cl_2. After neutralizing the aqueous phase with 5N NaOH, the organic phase was separated, washed with brine and dried over Na_2SO_4. The solvent was removed in vacuo yielding the free base ligand N4Py as a pink oil which was immediately used for the next step. $Fe(OTf)_2$·2 MeCN[33] (179 mg, 0.41 mmol) was then added to a solution of N4Py (140 mg, 0.38 mmol) in 5 mL tetrahydrofuran. After stirring for 14 h, hexane was added to afford a polycrystalline powder, which was then recrystallized from CH_2Cl_2/Et_2O. This compound was identified by its crystal structure (see Supporting Information) and by comparison of its ^1H NMR spectrum with that of **1b**$(ClO_4)_2$.

XAS Sample Preparation. A solid sample of **1b**$(ClO_4)_2$ (2 mg in 98 mg boron nitride) was prepared by grinding the two components into a homogeneous mixture under an inert gas atmosphere. 20 mg of the solid mixture were then packed into a sample plate (1 mm thick) and covered with Mylar tape.

Samples of the alkylperoxoiron(III) intermediates **2a** and **2b** were generated by addition of *tert*-BuO_2H to pre-cooled solutions of the respective iron(II) precursors. After a suitable reaction time during which the chromophore was observed to maximize by UV−visible spectroscopy, ca. 0.5 mL of the solution was transferred into a pre-cooled sample holder, covered with Mylar tape, which was then submerged in liquid nitrogen. EPR samples of **2a** and **2b** were prepared simultaneously from the same batches to assess what fraction of the XAS samples the intermediates represent.

$[Fe^{III}(TPA)(OO^tBu)(solv)]^{2+}$, 2a. 1a$(ClO_4)_2$, 10 mM in MeCN, −40 °C, + 10 equiv *tert*-BuO_2H (70% aqueous solution), reaction time 20 min; 65% by EPR double integration.

$[Fe^{III}(N4Py)(OO^tBu)]^{2+}$, 2b. 1b$(OTf)_2$, 5 mM in MeOH, −70 °C, + 10 equiv *tert*-BuO_2H (5 M in nonane), reaction time 12 h; 95% by EPR double integration.

Samples of the mononuclear oxoiron(IV) intermediates **3a**−**3c** were generated by the addition of the appropriate oxidant to a pre-cooled solution of the appropriate iron(II) precursor complex at the appropriate temperature as described below. Formation of the intermediate was followed by UV−visible spectroscopy. After 10 min ca. 0.5 mL of the solution with **3a**, **3b**, or **3c** was transferred into a pre-cooled tandem Mössbauer/XAS cup,[34] covered with Mylar tape, which was then submerged in liquid nitrogen.

$[Fe^{IV}(O)(TPA)(solv)]^{2+}$, 3a. To a solution of $[Fe(TPA)(OTf)_2]$ (0.018 mmol Fe, 33% ^{57}Fe) in 3 mL MeCN and 10 μL H_2O (doubly deionized, Milli-Q Water System, Millipore) in a UV−visible cuvette and pre-cooled to −40 °C was added a solution of 1.5 equiv AcO_2H (0.027 mmol, 32 wt. % AcO_2H) in 100 μL MeCN. (Note: Dissolution of $[Fe(TPA)(OTf)_2]$ in MeCN readily afforded the low-spin $[Fe(TPA)(NCMe)_2]^{2+}$ ion (**1a**), whose NMR spectrum was indistinguishable from that of **1a**$(ClO_4)_2$.) Mössbauer analysis of this sample showed 80(5) % formation of **3a**.

(18) Abbreviations used: Bn-TPEN, *N*-benzyl-*N*′, *N*′, *N*′-tris(2-pyridylmethyl)-1,2-diaminoethane; $HS^{Me2}N_4$(tren), 3-[*N*-[2-[*N*, *N*-bis(2-aminoethyl)amino]-ethyl]imino]-2-methyl-2-butanethiol; N4Py, *N*, *N*-bis(2-pyridylmethyl)-*N*-bis(2-pyridyl)methylamine; OTf, trifluoromethylsulfonate or triflate anion; $PaPy_3H$, *N*-[2-(*N*, *N*-bis(2-pyridylmethyl)amino)ethyl]pyridine-2-carboxamide; pyO, pyridine *N*-oxide; TMC, 1, 4, 8, 11-tetramethyl-1, 4, 8, 11-tetraazacyclotetradecane or tetra(*N*-methyl)cyclam; TPA, *N*,*N*,*N*-tris(2-pyridylmethyl)amine; EXAFS, extended X-ray absorption fine structure; XANES, X-ray absorption near-edge structure; XAS, X-ray absorption spectroscopy.

(19) Roelfes, G.; Vrajmasu, V.; Chen, K.; Ho, R. Y. N.; Rohde, J.-U.; Zondervan, C.; la Crois, R. M.; Schudde, E. P.; Lutz, M.; Spek, A. L.; Hage, R.; Feringa, B. L.; Münck, E.; Que, L., Jr. *Inorg. Chem.* **2003**, *42*, 2639−2653.
(20) Bukowski, M. R.; Zhu, S.; Koehntop, K. D.; Brennessel, W. W.; Que, L., Jr. *J. Biol. Inorg. Chem.* **2004**, *9*, 39−48.
(21) Neese, F.; Solomon, E. I. *J. Am. Chem. Soc.* **1998**, *120*, 12829−12848.
(22) Lehnert, N.; Ho, R. Y. N.; Que, L., Jr.; Solomon, E. I. *J. Am. Chem. Soc.* **2001**, *123*, 8271−8290.
(23) Lehnert, N.; Ho, R. Y. N.; Que, L., Jr.; Solomon, E. I. *J. Am. Chem. Soc.* **2001**, *123*, 12802−12816.
(24) Lehnert, N.; Neese, F.; Ho, R. Y. N.; Que, L., Jr.; Solomon, E. I. *J. Am. Chem. Soc.* **2002**, *124*, 10810−10822.
(25) Rohde, J.-U.; In, J.-H.; Lim, M. H.; Brennessel, W. W.; Bukowski, M. R.; Stubna, A.; Münck, E.; Nam, W.; Que, L., Jr. *Science* **2003**, *299*, 1037−1039.
(26) Lim, M. H.; Rohde, J.-U.; Stubna, A.; Bukowski, M. R.; Costas, M.; Ho, R. Y. N.; Münck, E.; Nam, W.; Que, L., Jr. *Proc. Natl. Acad. Sci. U.S.A.* **2003**, *100*, 3665−3670.
(27) Kaizer, J.; Klinker, E. J.; Oh, N. Y.; Rohde, J.-U.; Song, W. J.; Stubna, A.; Kim, J.; Münck, E.; Nam, W.; Que, L., Jr. *J. Am. Chem. Soc.* **2004**, *126*, 472−473.
(28) Armarego, W. L. F.; Perrin, D. D. *Purification of Laboratory Chemicals*; Butterworth-Heinemann: Oxford, 1997.
(29) Zang, Y.; Kim, J.; Dong, Y.; Wilkinson, E. C.; Appelman, E. H.; Que, L., Jr. *J. Am. Chem. Soc.* **1997**, *119*, 4197−4205.
(30) Roelfes, G.; Lubben, M.; Chen, K.; Ho, R. Y. N.; Meetsma, A.; Genseberger, S.; Hermant, R. M.; Hage, R.; Mandal, S. K.; Young, V. G., Jr.; Zang, Y.; Kooijman, H.; Spek, A. L.; Que, L., Jr.; Feringa, B. L. *Inorg. Chem.* **1999**, *38*, 1929−1936.
(31) Lubben, M.; Meetsma, A.; Wilkinson, E. C.; Feringa, B.; Que, L., Jr. *Angew. Chem., Int. Ed. Engl.* **1995**, *34*, 1512−1514.
(32) Roelfes, G.; Lubben, M.; Leppard, S. W.; Schudde, E. P.; Hermant, R. M.; Hage, R.; Wilkinson, E. C.; Que, L., Jr.; Feringa, B. L. *J. Mol. Catal. A* **1997**, *117*, 223−227.
(33) Hagen, K. S. *Inorg. Chem.* **2000**, *39*, 5867−5869.
(34) Riggs-Gelasco, P. J.; Shu, L.; Chen, S.; Burdi, D.; Huynh, B. H.; Que, L., Jr.; Stubbe, J. *J. Am. Chem. Soc.* **1998**, *120*, 849−860.

[Fe^{IV}(O)(TPA)(pyO)]$^{2+}$, 3a′. To a solution of [Fe(TPA)(OTf)$_2$] (0.03 mmol Fe, 33% ^{57}Fe) in 5 mL MeCN and pre-cooled to −40 °C was added a solution of 1.0 equiv AcO_2H (0.03 mmol, 32 wt. % AcO_2H) in 50 μL MeCN. After a reaction time of 5 min, 5 equiv pyO were added (sample transfer after 2 min). Mössbauer analysis showed a sample with 60(5) % **3a′**.

[Fe^{IV}(O)(N4Py)]$^{2+}$, 3b. To a solution of [Fe(N4Py)(NCMe)](ClO$_4$)$_2$, **1b**(ClO$_4$)$_2$, (0.027 mmol Fe, 33% ^{57}Fe) in 4.5 mL MeCN in a UV−visible cuvette at 25 °C were added 6 equiv AcO_2H (∼0.17 mmol, 32 wt. % AcO_2H). Mössbauer analysis showed a sample with 80(5) % **3b**.

[Fe^{IV}(O)(Bn-TPEN)]$^{2+}$, 3c. To a solution of [Fe(Bn-TPEN)(OTf)](OTf), **1c**(OTf), (0.05 mmol Fe) in 2 mL MeCN at 25 °C was added excess solid PhIO. The resulting mixture was stirred for 30 min and filtered. Its absorbance (λ_{max} = 740 nm) showed 85(5) % formation of **3c**.

Physical Methods. UV−visible spectra were recorded on an HP 8453A diode array spectrometer with samples maintained at low temperature using a cryostat from Unisoku Scientific Instruments, Japan. ^{1}H NMR spectra were recorded on a Varian Inova VXR-300 or Varian Inova VI-300 spectrometer at ambient temperature. Chemical shifts (ppm) were referenced to the residual solvent peaks. EPR spectra were recorded at X-band microwave frequency on a Bruker E−500 spectrometer equipped with an Oxford liquid He cryostat. Spin quantification of the S = 1/2 Fe^{III} signals was performed by double integration of the EPR first derivative signal recorded under nonsaturating conditions at 20 K for comparison with a Cu^{II}(EDTA) solution as a standard.

X-ray Absorption Spectroscopy. Data Collection. XAS data were collected at the Stanford Synchrotron Radiation Laboratory (SSRL) of the Stanford Linear Accelerator Center, beamline 7−3, and at the National Synchrotron Light Source (NSLS) of the Brookhaven National Laboratory, beamline X9B. Fe K-edge X-ray absorption spectra were recorded on frozen solutions at 5−15 K over the energy range 6.9−8.0 keV as described previously.[35,36] Storage ring conditions: 3 GeV, 50−100 mA (SSRL), and 2.8 GeV, 100−300 mA (NSLS). The beam vertical aperture of the pre-monochromator slits was 1 mm. Contamination of higher harmonics radiation was minimized by detuning the Si(220) double-crystal monochromator by 50% at ∼8 keV (beamline 7−3 at SSRL) and by a harmonic rejection mirror (beamline X9B at NSLS), respectively. The horizontal spot size on the sample was 4−5 mm in most cases. Spectra were measured with 10 eV steps below the edge, 0.3 eV steps in the edge region, and steps equivalent to 0.05 Å^{-1} increments above the edge (region borders were 6880, 7090, and 7140 eV at beamline 7−3, SSRL, and 6932, 7102, and 7137 eV at beamline X9B, NSLS). An iron foil spectrum was recorded concomitantly for internal energy calibration and the first inflection point of the K-edge was assigned to 7112.0 eV. The data were obtained as fluorescence excitation spectra (A_{exp} (C_f/C_0)) using a solid-state germanium detector (Canberra).

The Fe concentration in the samples and the number of scans acquired for each sample were as follows: **1b**, 70 mM Fe, 2 scans (beamline X9B at NSLS, 13 element detector); **2a**, 10 mM Fe, 2 independent samples, 13 scans, 14 scans (X9B at NSLS, 13 element detector); **2b**, 5 mM Fe, 7 scans (7−3 at SSRL, 30 element detector); **3a**, 6 mM Fe, 2 independent samples, 10 scans (X9B at NSLS, 13 element detector), 10 scans (7−3 at SSRL, 30 element detector); **3a′**, 6 mM Fe, 10 scans (7−3 at SSRL, 30 element detector); **3b**, 6 mM Fe, 10 scans (X9B at NSLS, 13 element detector); **3c**, 25 mM Fe, 3 scans (X9B at NSLS, 13 element detector).

Data Analysis. The treatment of raw EXAFS data to yield $\chi(k)$ is discussed in detail in review articles.[37,38] XAS data from beamline 7−3 at SSRL were calibrated and averaged with the program EXAFSPAK.[39] A background was then removed by fitting a Gaussian to the preedge region, extrapolating and subtracting this from the entire spectrum. A three-segment spline with fourth-order polynomial components was fit to the EXAFS region. The resulting EXAFS data in k space were Gaussian smoothed. Curve-fitting of XANES data to obtain preedge peak areas and fitting of EXAFS data were carried out with the program SSExafs according to a previously described protocol.[35,40] XAS data from beamline X9B at NSLS were treated entirely with SSExafs. Here, baseline subtraction and determination of the edge height were accomplished by fitting a cubic spline function (equally spaced throughout the EXAFS region) simultaneously with edge and EXAFS parameters (including first-shell parameters), and a correction of fluorescence data for thickness effects. We have made comparisons using both software packages EXAFSPAK and SSExafs for calibration and background subtraction; the different protocols, however, did not lead to any systematic errors and the results were identical within the error of analysis.

The edge was modeled as an integral of a 75% Gaussian and 25% Lorentzian peak. The heights, positions and widths (at half-height) of preedge peaks were refined using a Gaussian function. Refinements with multiple peaks were constrained to have a common width for all peaks. Preedge peak areas are in % of Fe K-edge height (eV) and were multiplied by 100.

The EXAFS refinements reported were on $k^3\chi(k)$ data and the function minimized was $R = \{\Sigma\, k^6(\chi_c - \chi)^2/N\}^{1/2}$, where the sum is over N data points within the selected k space. Single-scattering EXAFS theory allows the total EXAFS spectrum to be described as the sum of shells of separately modeled atoms, e.g., $\chi_c = \Sigma\, nA[f(k)k^{-1}r^{-2}\exp(-2\sigma^2k^2)\sin(2kr + \alpha(k))]$, where n is the number of atoms in the shell, $k = [8\pi^2m_e(E - E_0 + \Delta E)/h^2]^{1/2}$, and σ^2 is the Debye−Waller factor.[35] The amplitude reduction factor (A) and the shell-specific edge shift (ΔE) are empirical parameters that partially compensate for imperfections in the theoretical amplitude and phase functions.[41] Phase and amplitude functions were theoretically calculated using a curved-wave formalism.[42] A variation of FABM (fine adjustment based on models) was used here in the analysis procedure with theoretical phase and amplitude functions.[43] In each shell, two parameters were refined at one time (r and n or σ^2), while A and ΔE values were determined by using a series of crystallographically characterized model complexes. The fitting results indicate the average metal−ligand distances, the type and the number of scatterers, and the Debye−Waller factors which can be used to evaluate the distribution of Fe-ligand bond lengths in each shell. The EXAFS goodness of fit criterion applied here is

$$\epsilon^2 = [(N_{idp}/\nu)\cdot\Sigma\,(\chi_c - \chi)^2/{\sigma_{data}}^2]/N$$

as recommended by the International Committee on Standards and Criteria in EXAFS[44,45] where ν is the number of degrees of freedom calculated as $\nu = N_{idp} - N_{var}$, N_{idp} is the number of independent data points, N_{var} is the number of variables that are refined, and σ_{data} is the estimated uncertainty of the data (usually set at 1). N_{idp} is calculated as

(35) Scarrow, R. C.; Maroney, M. J.; Palmer, S. M.; Que, L., Jr.; Roe, A. L.; Salowe, S. P.; Stubbe, J. *J. Am. Chem. Soc.* **1987**, *109*, 7857−7864.
(36) Shu, L.; Chiou, Y.-M.; Orville, A. M.; Miller, M. A.; Lipscomb, J. D.; Que, L., Jr. *Biochemistry* **1995**, *34*, 6649−6659.
(37) Scott, R. A. *Methods Enzymol.* **1985**, *117*, 414−459.
(38) Teo, B.-K.; Joy, D. C. *EXAFS Spectroscopy: Techniques and Applications*; Plenum Press: New York, 1981.
(39) George, G. N.; Pickering, I. J.; Stanford Synchrotron Radiation Laboratory, Stanford Linear Accelerator Center, 2000.
(40) Scarrow, R. C.; Trimitsis, M. G.; Buck, C. P.; Grove, G. N.; Cowling, R. A.; Nelson, M. J. *Biochemistry* **1994**, *33*, 15023−15035.
(41) Teo, B.-K.; Lee, P. A. *J. Am. Chem. Soc.* **1979**, *101*, 2815−2832.
(42) McKale, A. G.; Veal, B. W.; Paulikas, A. P.; Chan, S.-K.; Knapp, G. S. *J. Am. Chem. Soc.* **1988**, *110*, 3763−3768.
(43) Teo, B.-K.; Antonio, M. R.; Averill, B. A. *J. Am. Chem. Soc.* **1983**, *105*, 3751−3762.
(44) Bunker, G. A.; Hasnain, S. S.; Sayers, D. E. In *X-ray Absorption Fine Structure*; Hasnain, S. S., Ed.; Ellis Horwood: New York, 1991; pp 751−770.
(45) Riggs-Gelasco, P. J.; Stemmler, T. L.; Penner-Hahn, J. E. *Coord. Chem. Rev.* **1995**, *144*, 245−286.

$N_{idp} = 2\Delta k\Delta R/\pi + 2$.[46] The use of ϵ^2 as the criterion for the goodness of fit allows us to compare fits using different numbers of variable parameters.

Fitting Procedure. Fitting parameters *A* (amplitude reduction factor) and ΔE (phase shift) for inner-sphere N/O and outer-sphere C scatterers had been extracted from Fe(acac)$_3$ (Fe−O, 1.986−2.004 Å; Fe···C, 2.935−2.971 Å).[35] Since backscatterers differing in *Z* by 1 unit cannot be distinguished by EXAFS, N and O scatterers were fit using the same parameters *A*, ΔE, and $Z = 7$ (assigned as N/O shell). However, $Z = 8$ was applied for the short-distance scatterer in **3a**, **3a′**, **3b**, and **3c**; the shell was denoted as O/N. Initially, inner-sphere shells were refined using the corresponding back-transformation range "b" (see Tables 3 and 4). Two of the parameters *n*, *r*, and $\Delta\sigma^2$ were allowed to float at the same time, while the third parameter had been kept fixed. Subsequently, these shells were refined across the broader window "c" and outer-sphere shells were included. The resolution was calculated from $\Delta r \approx \pi\,(2\,\Delta k)^{-1}$.[45] The typical error of analysis for interatomic distances (*r*) is approximately ±0.02 Å.[37,47]

Results

In this study, we have obtained Fe K-edge X-ray absorption spectra of seven low-spin iron complexes with oxidation states +II to +IV to gain structural insight into the changes in the iron coordination sphere as the metal center becomes oxidized concomitant with the introduction of peroxo or oxo ligands. Complexes of three supporting polydentate ligands have been investigated. Our detailed analyses are presented below.

I. Iron(II) Precursor Complexes. The neutral nitrogen ligands, tetradentate TPA and pentadentate N4Py and Bn-TPEN, represent a series of ligands with differing ratios of pyridine and amine functions that allow us to fine-tune the properties and stabilities of transient iron complexes. The precursors to such intermediates are six-coordinate iron(II) complexes of these ligands that have, depending on the denticity of the supporting ligand, one or two labile coordination sites: $[Fe^{II}(TPA)(NCMe)_2]^{2+}$, **1a**, $[Fe^{II}(N4Py)(NCMe)]^{2+}$, **1b**, and $[Fe^{II}(Bn\text{-}TPEN)(OTf)]^{+}$, **1c** (Figure 1). The Fe−N bond lengths in the crystal structures of $[Fe^{II}(TPA)(NCMe)_2](BPh_4)_2$,[29] **1a**$(BPh_4)_2$, $[Fe^{II}(N4Py)(NCMe)](ClO_4)_2$,[30] **1b**$(ClO_4)_2$, and $[Fe^{II}(N4Py)(NCMe)](OTf)_2$, **1b**$(OTf)_2$ (see Supporting Information) lie in the range of 1.915−1.989 Å (Table S1), typical for low-spin iron(II) complexes. On the other hand, $[Fe^{II}(Bn\text{-}TPEN)(OTf)](OTf)$, **1c**(OTf), is high spin and the Fe−N bonds are longer, 2.032−2.236 Å (see Supporting Information, Table S1).

We have obtained XAS data of **1b**$(ClO_4)_2$ for comparison purposes to take advantage of the fact that its crystal structure shows a nearly octahedral FeN_6 environment with very similar Fe−N bond lengths. The EXAFS spectrum can be best fit with 5 nitrogen scatterers at an Fe−N distance of 1.96 Å (Table S2, Figure S4). This distance represents the average of the six Fe−N distances. The underestimated *n* value and the resulting Debye−Waller factor arise from reduction in the scattering amplitude in the EXAFS spectrum, reflecting the static and/or dynamic disorder inherent in the first coordination sphere; i.e., the Fe−N_{NCMe} distance of 1.915 Å in the crystal structure is shorter by ca. 0.05 Å than the average Fe−N_{N4Py} distance. On the other hand, these distances are too close to be resolved by EXAFS into two individual shells (Table S2).

II. Formation and Properties of Intermediates. A. Alkylperoxoiron(III) Intermediates. Iron(II) precursors **1a** and **1b** react with *tert*-BuO_2H at low temperature to form metastable alkylperoxoiron(III) complexes $[Fe^{III}(TPA)(OO^tBu)(solv)]^{2+}$,[29] **2a**, and $[Fe^{III}(N4Py)(OO^tBu)]^{2+}$, **2b** (Scheme 1). These intermediates have different thermal stabilities. While **2a** is readily observable in MeCN at −40 °C, **2b** could only be obtained at temperatures below −60 °C. To do so, **1b**$(OTf)_2$ was synthesized to enhance the solubility of this complex in solvents with lower-temperature melting points than MeCN. As shown in Figure 2, addition of *tert*-BuO_2H at −70 °C to a solution of **1b**$(OTf)_2$ in CH_2Cl_2 results in the disappearance of absorption features characteristic of **1b** and the concomitant isosbestic formation of an intense new chromophore **2b** with λ_{max} at 560 nm ($\epsilon = 2400\ M^{-1}cm^{-1}$); similar results are obtained in MeOH,

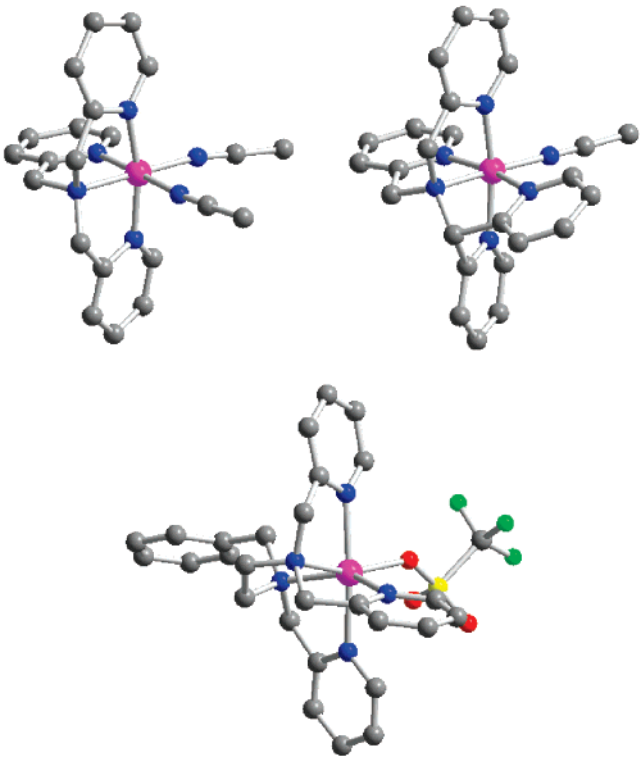

Figure 1. Molecular structures of complex cations in $[Fe^{II}(TPA)(NCMe)_2](BPh_4)_2$, **1a**$(BPh_4)_2$ (top left), $[Fe^{II}(N4Py)(NCMe)](ClO_4)_2$·MeOH, **1b**$(ClO_4)_2$·MeOH (top right), and $[Fe^{II}(Bn\text{-}TPEN)(OTf)](OTf)$, **1c**(OTf) (bottom); color key: pink = Fe, blue = N, gray = C, red = O, yellow = sulfur, green = fluorine.

Scheme 1. Generation and Interconversion of Alkylperoxoiron(III) Complexes (**2**) and Oxoiron(IV) Complexes (**3**)[a]

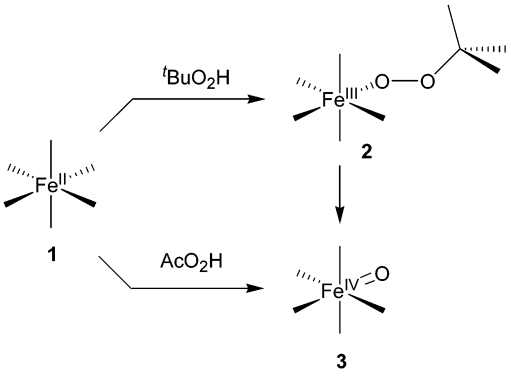

[a] The **1** → **3** conversion was realized for **1a**, in MeCN, −40 °C; for **1b**, in MeCN, 25 °C; for **1c**, in MeCN, −20 °C; **1** → **2** for **1a**, in MeCN, −40 °C; for **1b**, in CH_2Cl_2 or MeOH, −70 °C; **2** → **3** for **2a**, in MeCN, −25 °C.

(46) Stern, E. A. *Phys. Rev.* **1993**, *B48*, 9825−9827.
(47) Penner-Hahn, J. E. *Coord. Chem. Rev.* **1999**, *190*−*192*, 1101−1123.

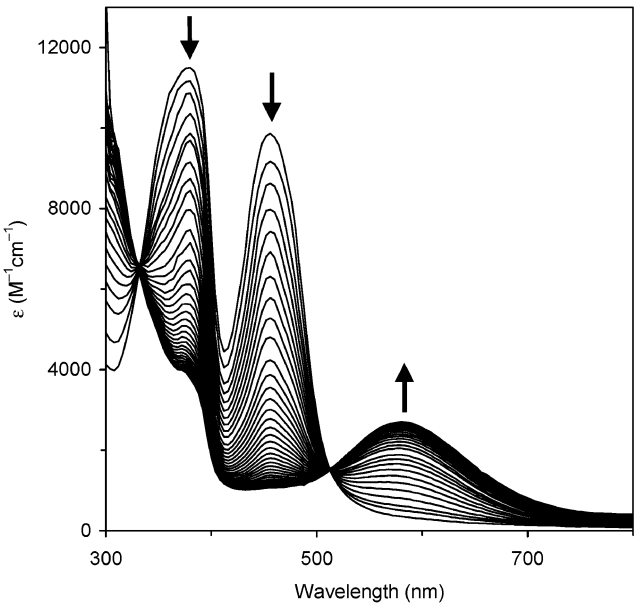

Figure 2. Conversion of 1 mM **1b** (—) to **2b** (—) in CH_2Cl_2 at −70 °C by addition of 10 equiv *tert*-BuO_2H, as monitored by UV−visible spectroscopy.

Table 1. Optical and Mössbauer Properties of $[Fe^{IV}(O)(TMC)(NCMe)]^{2+}$,[25] **3a**, **3a′**, **3b**, and **3c**

	λ_{max} (nm) (ϵ (M^{-1}·cm^{-1}))	δ (mm·s^{-1})	ΔE_Q (mm·s^{-1})
$[Fe^{IV}(O)(TMC)(NCMe)]^{2+}$	820 (400)	0.17	1.24
3a	724 (300)	0.01	0.92
3a′	742 (300)	0.04	0.90
3b	695 (400)	−0.04	0.93
3c	740 (400)	0.01	0.87

which is more suitable for XAS studies. Like **2a**, **2b** also exhibits an EPR spectrum with *g* values at 2.16, 2.10 and 1.97, indicative of a low-spin iron(III) center. As previously established for **2a** (λ_{max} at 600 nm; $\epsilon = 2200$ $M^{-1}cm^{-1}$), low-spin alkylperoxoiron(III) complexes have deep blue colors that arise from an alkylperoxo-to-iron(III) charge-transfer transition.[22,29] The different thermal stabilities of **2a** and **2b** may relate to the differences in the sixth ligand. The sixth ligand in **2b** is presumably the additional pyridine in the N4Py ligand framework relative to TPA, while that for **2a** is most likely MeCN. We have previously demonstrated that coordination of pyridine as the sixth ligand to **2a** significantly diminishes its thermal stability at −40 °C.[48]

B. Oxoiron(IV) Intermediates. The oxoiron(IV) intermediates **3a**, **3b**, and **3c** can be obtained from the reaction of AcO_2H with their iron(II) precursors **1a**, **1b**, and **1c**.[26,27] These intermediates are pale green species with absorption maxima in the near-IR region (Table 1) whose formulations as $[Fe^{IV}(O)(L)]^{2+}$ ions have been established by electrospray ionization mass spectrometry. They are EPR silent and exhibit Mössbauer properties that compare well with those reported for crystallographically characterized $[Fe^{IV}(O)(TMC)(NCMe)](OTf)_2$ and are characteristic of a mononuclear $S = 1$ iron(IV) center in a nitrogen-rich ligand environment.[25] Because of their different thermal stabilities, **3a**−**3c** require different temperatures for their generation procedure: −40 °C for **3a**, 25 °C for **3b**, and −20 °C for **3c**. The latter two can also be formed conveniently by the reaction of **1b** or **1c** with excess solid PhIO at 25 °C in MeCN. In fact, the XAS sample of **3c** for this study was obtained by the use of the latter reagent. In addition, pyridine *N*-oxide was added to a solution of **3a** in MeCN to afford **3a′** with the MeCN replaced by pyridine *N*-oxide as the sixth ligand. The coordination of pyridine *N*-oxide to the oxoiron(IV) center is indicated by the red shift of its near-IR absorption feature to 742 nm. This collection of novel intermediates is the focus of this XAS structural study.

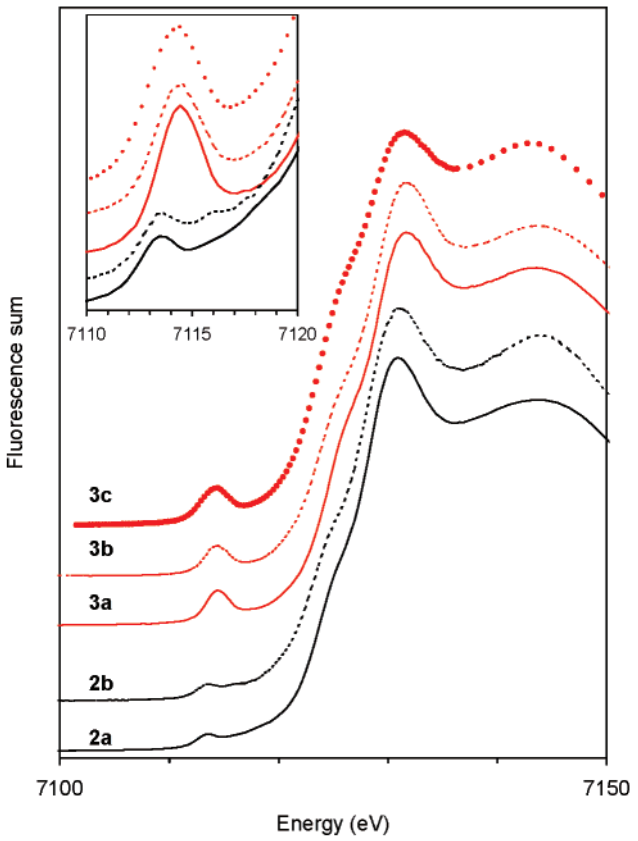

Figure 3. Fe K-edge X-ray absorption near-edge structures (XANES, fluorescence excitation) of iron(III) complexes $[Fe^{III}(TPA)(OO^tBu)(solv)]^{2+}$, **2a** (—), and $[Fe^{III}(N4Py)(OO^tBu)]^{2+}$, **2b** (- - -); and iron(IV) complexes $[Fe^{IV}(O)(TPA)(solv)]^{2+}$, **3a** (red —), $[Fe^{IV}(O)(N4Py)]^{2+}$, **3b** (red - - -), and $[Fe^{IV}(O)(Bn\text{-}TPEN)]^{2+}$, **3c** (red ···).

III. X-ray Absorption Near-Edge Structures. A. Alkylperoxoiron(III) Intermediates. X-ray absorption spectra at the Fe K-edge were measured for two alkylperoxoiron(III) complexes with different supporting ligands. The near-edge structures of $[Fe^{III}(TPA)(OO^tBu)(solv)]^{2+}$, **2a**, and $[Fe^{III}(N4Py)(OO^tBu)]^{2+}$, **2b**, are shown in Figure 3. The position of the rising K-edge, where a 1s electron is promoted to the continuum, depends on the effective charge of the metal center and is thus related to the oxidation state, but is also influenced by the ligand environment of the metal center. The Fe K-edges of **2a** and **2b** exhibit similar shapes and lie at similar energies (based on the first inflection point, Table 2). Relative to **1b**, their edges upshift by ca. 1.5 eV, consistent with their higher oxidation state.

The preedge regions of **2a** and **2b** magnified in the inset of Figure 3 consist of 1s→3d transitions, as observed for many iron(III) complexes,[49−51] and can be fit with a minimum of two features with energies and peak areas listed in Table 2. The major component is a prominent peak at ca. 7113.5 eV that is

(48) Kaizer, J.; Costas, M.; Que, L., Jr. *Angew. Chem., Int. Ed.* **2003**, *42*, 3671−3673.

Table 2. XAS Preedge Peak Energies and Intensities for the Iron Complexes in This Study[a]

complex	E_0 (eV)	$E_{preedge}$ (eV)	area
1b	7122.0	7112.9	3.9(3)
2a	7123.6	7113.4	7.2(3)
		7115.9	1.7(2)
2b	7123.4	7113.5	9.7(3)
		7116.0	5.3(3)
3a	7124.5	7114.4	25.4(3)
3a′	7124.8	7114.6	24.5(4)
3b	7123.7	7114.3	25.2(5)
3c	7123.7	7114.1	29.3(4)

[a] E_0 is conventionally defined as the first inflection point of the edge and used as the reference point for the *k*-space spectrum. This choice is somewhat arbitrary, but does not significantly affect metal−ligand distances. Preedge peak energies and intensities were determined by curve fitting to the data as described.[40,50] Intensities are reported as peak areas (normalized to the edge jump) and were multiplied by 100.

readily observed for both complexes. The minor component found at ca. 7116 eV is easily seen only for **2b** in Figure 3 inset, while the less intense minor component of **2a** can be discerned in the background-subtracted spectrum shown in Figure S8 (Supporting Information). Intermediates **2a** and **2b** exhibit total preedge areas of 9(1) and 15(1) units, respectively, values higher than those found for centrosymmetric six-coordinate iron complexes.[49−51] The higher intensity can be ascribed to the expected lower symmetry of the iron sites in the alkylperoxo complexes due to the presence of the unique Fe−OO^{t}Bu bond, which should be much shorter than the Fe−N bonds (2.0 Å). The distortion from centrosymmetry increases the mixing of $3d_{z2}$ and $4p_z$ orbitals (*z* axis defined as the direction of the Fe−OO^{t}Bu bond) and thus gives rise to more intense preedge features.

B. Oxoiron(IV) Intermediates. The near-edge structures of the Fe K-edge X-ray absorption spectra (XANES) of oxoiron(IV) complexes $[Fe^{IV}(O)(TPA)(solv)]^{2+}$, **3a**, $[Fe^{IV}(O)(N4Py)]^{2+}$, **3b**, and $[Fe^{IV}(O)(Bn\text{-}TPEN)]^{2+}$, **3c**, are shown in Figure 3. The K edges of **3a**, $[Fe^{IV}(O)(TPA)(pyO)]^{2+}$ (**3a′**), **3b** and **3c** are shifted to higher energies as compared to those of corresponding iron(III) complexes **2a** and **2b**, due to the increase in oxidation state, but the effect is small. More importantly, **3a**, **3a′**, **3b**, and **3c** exhibit intense 1s→3d preedge transitions with areas of 25−30 units (Table 2).[52] Such high values have been observed for crystallographically characterized $[Fe^{IV}(O)(TMC)(NCMe)](OTf)_2$ (30(4) units),[26] and for oxoiron(IV) porphyrin complexes (27−38 units).[53,54] The occurrence of an intense 1s→3d preedge transition indicates significant mixing of 3d and 4p orbitals. This may be caused by strong Fe=O π bonding that leads to the large deviation from centrosymmetry of the iron ligand field imposed by a terminal oxo ligand. The strong covalency of the Fe=O bond[55] may also provide the rationale for the rather small upshift of the K-edges in the Fe^{IV}=O complexes relative to that of the Fe^{III}−OOR intermediates.

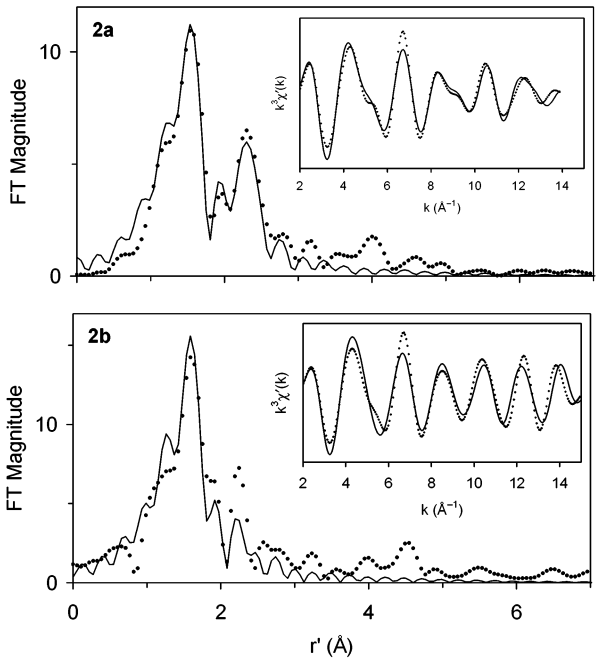

Figure 4. Fourier transforms of the Fe K-edge EXAFS data ($k^3\chi(k)$) and Fourier-filtered EXAFS spectra ($k^3\chi'(k)$, inset) of $[Fe^{III}(TPA)(OO^tBu)(solv)]^{2+}$, **2a**, Fourier transformed range $k = 2-13.9$ Å^{-1}; experimental data (···) and fit 1 N/O, 4 N/O, 6 C, (—); Back-transformation range: $r' = 0.60-3.40$ Å (top); and of $[Fe^{III}(N4Py)(OO^tBu)]^{2+}$, **2b**, Fourier transformed range $k = 2-15$ Å^{-1}; experimental data (···) and fit 1 N/O, 5 N/O, 3 C, (—); Back-transformation range: $r' = 0.60-3.10$ Å (bottom).

IV. EXAFS Spectra and Fitting Results. A. Alkylperoxoiron(III) Intermediates. The Fourier transforms (r' space) of the Fe K-edge EXAFS data of alkylperoxoiron(III) complexes **2a** and **2b** exhibit prominent features centered at $r' = 1.6$, 2.0, and 2.3 Å with a shoulder at 1.2 Å (Figure 4), where r' corresponds to the actual metal-scatterer distance r after a phase shift correction of approximately 0.4 Å ($r \approx r' + 0.4$ Å). The first coordination spheres of the low-spin iron(III) centers of these complexes can be fit well by two shells of N/O atoms at absorber-scatterer distances (r) of 1.78 and 1.96−1.97 Å. The shorter-distance shell corresponds to the oxygen scatterer of the Fe−OO^{t}Bu moiety. This short Fe−O distance undoubtedly arises from π interactions that stengthen the Fe−O bond,[22] as also found in the crystal structure of $[Fe^{III}(N4Py)(OMe)]^{2+}$ [30] and the EXAFS analysis for $[Fe^{III}(N4Py)(OOH)]^{2+}$.[19]

The shell at ca. 2.0 Å with 4 or 5 scatterers represents the donor nitrogen atoms of the polydentate ligands TPA and N4Py (Table 3). This distance is comparable to the average Fe−N bond lengths in low-spin Fe^{III} complexes of pyridine and/or tertiary amine ligands.[29,56−59] For **2a**, good fits are achieved with either 4 or 5 N/O atoms at 1.96 Å; the fit with 4 N/O atoms affords a lower goodness-of-fit (GOF) value (Table 3, fits 3 and 4).[60] Besides the ligating nitrogens of the tetradentate TPA ligand, the donor atom of a sixth ligand, possibly a solvent molecule MeCN, may contribute to this shell, as the low-spin

(49) Roe, A. L.; Schneider, D. J.; Mayer, R. J.; Pyrz, J. W.; Widom, J.; Que, L., Jr. *J. Am. Chem. Soc.* **1984**, *106*, 1676−1681.
(50) Randall, C. R.; Shu, L.; Chiou, Y.-M.; Hagen, K. S.; Ito, M.; Kitajima, N.; Lachicotte, R. J.; Zang, Y.; Que, L., Jr. *Inorg. Chem.* **1995**, *34*, 1036−1039.
(51) Westre, T. E.; Kennepohl, P.; DeWitt, J. G.; Hedman, B.; Hodgson, K. O.; Solomon, E. I. *J. Am. Chem. Soc.* **1997**, *119*, 6297−6314.
(52) We first reported **3a** to have a preedge peak area of 30 units but have revised this value downwards upon further study.
(53) Wolter, T.; Meyer-Klaucke, W.; Müther, M.; Mandon, D.; Winkler, H.; Trautwein, A. X.; Weiss, R. *J. Inorg. Biochem.* **2000**, *78*, 117−122.
(54) Nam, W.; Choi, S. K.; Lim, M. H.; Rohde, J.-U.; Kim, I.; Kim, J.; Kim, C.; Que, L., Jr. *Angew. Chem., Int. Ed.* **2003**, *42*, 109−111.
(55) Decker, A.; Rohde, J.-U.; Que, L., Jr.; Solomon, E. I. *J. Am. Chem. Soc.* **2004**, *126*, 5378−5379.
(56) Baker, J.; Engelhardt, L. M.; Figgis, B. N.; White, A. H. *J. Chem. Soc., Dalton Trans.* **1975**, 530−534.
(57) Figgis, B. N.; Skelton, B. W.; White, A. H. *Aust. J. Chem.* **1978**, *31*, 57−64.
(58) Marsh, R. E. *Acta Crystallogr.* **1987**, *B43*, 174−178.
(59) Duelund, L.; Hazell, R.; McKenzie, C. J.; Preuss Nielsen, L.; Toftlund, H. *J. Chem. Soc., Dalton Trans.* **2001**, 152−156.

Table 3. EXAFS Fitting Results for $[Fe^{III}(TPA)(OO^tBu)(solv)]^{2+}$, **2a**, and $[Fe^{III}(N4Py)(OO^tBu)]^{2+}$, **2b**[a]

		Fe–N/O			Fe–N/O			Fe···C			GOF	
complex	fit	*n*	*r* (Å)^2	$\Delta\sigma^2$	*n*	*r* (Å)^2	$\Delta\sigma^2$	*n*	*r* (Å)^2	$\Delta\sigma^2$	$\epsilon^2 \cdot 10^3$[b]	*c*
2a	1				5	1.95	5.6				0.70	
	2				4	1.95	3.7				0.65	
	3	1	1.74	5	5	1.96	4.3				0.62	
	4	1	1.79	4	4	1.96	2.4				0.52	
	5				5	1.95	5.6					1.25
	6	1	1.79	3	4	1.96	2.4					1.19
	7	**1**	**1.78**	**2.9**	**4**	**1.96**	**2.3**	**6**	**2.84**	**3.5**		**0.67**
	(*7*	*1*	*1.78*	*3.7*	*4*	*1.96*	*2.5*	*6*	*2.83*	*3.6*		*0.80*)[d]
	8				4	1.95	3.7	6	2.83	3.6		0.80
2b	1				6	1.96	3.8				1.21	
	2	1	1.77	1.1	5	1.96	1.7				0.83	
	3				6	1.96	3.7					1.48
	4	1	1.78	0.5	5	1.97	1.5					1.19
	5	1	1.78	0.4	5	1.97	1.5	4	2.83	7		1.12
	6	**1**	**1.78**	**0.4**	**5**	**1.97**	**1.5**	**3**	**2.82**	**6**		**1.13**
	(*6*	*1*	*1.78*	*1.2*	*5*	*1.97*	*1.7*	*3*	*2.81*	*6.1*		*1.33*)[d]
	7				5	1.96	2.3	3	2.82	6		1.33

[a] Fourier transformed range for **2a**: $k = 2-13.9$ Å^{-1} (resolution 0.13 Å); for **2b**: $k = 2-15$ Å^{-1} (resolution 0.12 Å). *r* is in units Å, $\Delta\sigma^2$ in 10^3 Å^2. Back-transformation range for **2a**: [b] $r' = 0.60-2.10$ Å; [c] $r' = 0.60-3.40$ Å; for **2b**: [b] $r' = 0.60-2.10$ Å; [c] $r' = 0.60-3.10$ Å. [d] Fits to unfiltered data corresponding to the best fits to filtered data.

nature of these complexes almost certainly requires the presence of a sixth ligand. The expected coordination number of $n = 5$ is consistent with this fit due to the limited accuracy for coordination numbers determined by EXAFS analysis (20−30%).[37,47] For **2b**, the low Debye−Waller factor, even with an occupancy of $n = 5$, reflects a small degree of static and vibrational disorder in the Fe−N bonds (Table 3, fit 2). In fact, N4Py is a quite constrained ligand. The crystallographically determined Fe−N distances in **1b**$(ClO_4)_2 \cdot$ MeOH (or **1b**$(OTf)_2$), fall in a very narrow range of 1.961−1.976 Å (1.970−1.983 Å for OTf salt, Table S1). The strong similarities of inner-sphere parameters between **2a** and **2b** are not surprising, because both intermediates are proposed to have a $[Fe^{III}N_5(OO^tBu)]^{2+}$ core.

Fits including the outer-sphere features reveal an Fe···C shell at approximately 2.8−2.9 Å. For **2b**, the inclusion of one shell of three carbon scatterers at 2.82 Å leads at best to only a minor improvement in GOF (Table 3, fit 6). An examination of the crystal structure of **1b**$(ClO_4)_2$ reveals that the carbon atoms adjacent to the ligating nitrogen atoms give rise to a wide range of Fe···C distances (2.650−3.023 Å, Table S1). Such a broad distribution of backscatterers would likely lead to some destructive interference, which is expected to decrease the amplitude of the associated components in the EXAFS spectrum. The possibility of splitting this feature into subshells is further complicated by the limitations of resolution ($\Delta r > \approx 0.12$ Å). The best fit to the Fourier-filtered EXAFS spectrum ($k^3\chi'(k)$) of **2b** consists of three shells: 1 N/O at 1.78 Å ($\Delta\sigma^2$, 0.0004 Å^2), 5 N/O at 1.97 Å (0.0015), and 3 C at 2.82 Å (0.006) (Table 3, fit 6, and Figure 4). These parameters are virtually the same as those of $[Fe^{III}(N4Py)(OOH)]^{2+}$,[19] strongly suggesting that these two peroxo intermediates have similar structures.

The outer-sphere contributions to the r' space spectrum of **2a** can be fit well with an Fe···C shell of 6 scatterers, significantly decreasing the GOF value and affording reasonable Debye−Waller factors ($\Delta\sigma^2$, Table 3, fit 7). Presumably, the smaller spread of Fe···C distances in **2a**, as evidenced in the crystal structure of its low-spin iron(II) precursor, **1a**$(BPh_4)_2$,[29] allows the backscattering contributions from this multi-carbon shell to combine constructively to afford the more intense outer-sphere features. Thus, like that of **2b**, the spectrum of **2a** can be fit well with three shells: 1 N/O at 1.78 Å ($\Delta\sigma^2$, 0.0029 Å^2), 4 N/O at 1.96 Å (0.0023), and 6 C at 2.84 Å (0.0035) (Table 3, fit 7, and Figure 4).

B. Oxoiron(IV) Intermediates. The Fourier transforms (r' space) of the Fe K-edge EXAFS data of oxoiron(IV) complexes **3a**, **3a′**, **3b**, and **3c** exhibit a single prominent feature in the region of $r' = 1.5-1.6$ Å and peaks of much lower intensity in the region of 2.2−2.5 Å (Figures 5 and S7). Interestingly, unlike in the spectra of the alkylperoxoiron(III) intermediates discussed in the previous section, a shoulder at 1.2 Å is not observed in the spectra of the oxoiron(IV) complexes (see also Figure S3). Simulations of the first coordination sphere of the iron center require two shells at 1.65−1.68 and 1.97−2.00 Å (Table 4). The principal shell at ca. 2.0 Å consisting of 4 or 5 N/O atoms is ascribed to the donor nitrogen atoms of the polydentate ligands (TPA, N4Py, Bn-TPEN) as in the corresponding iron(III) complexes. The other shell at ca. 1.65 Å consists of a single O/N atom and its introduction results in significant decreases in the GOF values of the spectral fits for all four complexes. This very short absorber-scatterer distance, much shorter than the 1.8-Å Fe−OOR distance in the alkylperoxoiron(III) complexes, arises from the terminal Fe═O group, in excellent agreement with the 1.646 Å Fe═O distance found in the crystallographically characterized $[Fe^{IV}(O)(TMC)(NCMe)](OTf)_2$ (1.646(3) Å),[25,61] and in oxoiron(IV) porphyrin complexes (1.60−1.70 Å) deduced from EXAFS analysis (synthetic porphyrins and horseradish peroxidase compounds I and II).[53,54,62−65]

The EXAFS spectrum of **3a** can be sufficiently described by three shells: 1 O/N at 1.65 Å ($\Delta\sigma^2$, 0.0003 Å^2), 4 N/O at 1.98 Å (0.0024), and 6 C at 2.89 Å (0.0038) (Table 4, fit 10, and Figure 5). A fourth absorber-scatterer shell can be refined to a distance at ca. 2.14 Å. Inclusion of this shell models better the beat feature at $k \approx 5$ Å^{-1} in the observed EXAFS spectrum (Table 4, fit 11, and Figure S6), but does not improve the global fit (see GOF value). Analysis of an earlier independent sample of **3a** with a poorer signal-to-noise ratio, however, required a four-shell fit with a subshell at 2.20 Å (Table S7, fit 11; see also ref 26). This sample contains approximately 80% of an $S = 1$ Fe^{IV} species and 18% of a high-spin Fe^{III} decay product, $[Fe^{III}_2(\mu\text{-}O)(\mu\text{-}OAc)(TPA)_2]^{3+}$, according to Mössbauer analysis. The 4 N/O scatterers at 1.99 Å may then be attributed to nitrogen atoms of TPA ligated to Fe^{IV}, and the single-scatterer shell at 2.20 Å to the Fe−N distance in the high-spin Fe^{III} decay product.[66] Assignment of the 2.20-Å shell to the high-spin Fe^{III}

(60) The 1.8-Å shell in the two samples of **2a** could also be fit with an occupancy lower than $n = 1$ (Tables S3 and S4), consistent with the lower conversion evidenced by the intensity of the EPR signals in the $g = 2$ region that account for 65% of the Fe in a simultaneously prepared sample.

(61) We have tested our method of analysis by fitting the EXAFS spectrum of crystallographically characterized $[Fe(O)(TMC)(NCMe)](OTf)_2$ and were able to obtain Fe−O and Fe−N distances in excellent agreement with the values from the crystal structure determination. Details of this analysis will be presented in a separate study currently in preparation.

(62) Penner-Hahn, J. E.; McMurry, T. J.; Renner, M.; Latos-Grazynsky, L.; Eble, K. S.; Davis, I. M.; Balch, A. L.; Groves, J. T.; Dawson, J. H.; Hodgson, K. O. *J. Biol. Chem.* **1983**, *258*, 12761−12764.

(63) Penner-Hahn, J. E.; Eble, K. S.; McMurry, T. J.; Renner, M.; Balch, A. L.; Groves, J. T.; Dawson, J. H.; Hodgson, K. O. *J. Am. Chem. Soc.* **1986**, *108*, 7819−7825.

Table 4. EXAFS Fitting Results for $[Fe^{IV}(O)(TPA)(solv)]^{2+}$, **3a**, $[Fe^{IV}(O)(TPA)(pyO)]^{2+}$, **3a′**, $[Fe^{IV}(O)(N4Py)]^{2+}$, **3b**, and $[Fe^{IV}(O)(Bn\text{-}TPEN)]^{2+}$, **3c**[a]

		Fe–O/N			Fe–N/O			Fe–N/O			Fe···C			GOF	
complex	fit	*n*	*r* (Å)^2	$\Delta\sigma^2$	*n*	*r* (Å)^2	$\Delta\sigma^2$	n	*r* (Å)^2	$\Delta\sigma^2$	*n*	*r* (Å)^2	$\Delta\sigma^2$	$\epsilon^2 \cdot 10^3$ [b]	*c*
3a	1				6	1.99	6.3							1.57	
	2				5	1.98	4.1							1.38	
	3	1	1.65	−0.1	5	1.98	4.1							0.82	
	4	1	1.65	0.2	4	1.98	2.5							0.71	
	5	1	1.65	0.4	4	1.98	2.2	1	2.18	8				0.70	
	6				5	1.98	4.1								1.58
	7	1	1.66	0.1	5	1.98	4.1								1.19
	8	1	1.65	0.4	4	1.98	2.4								1.14
	9	**1**	**1.65**	**0**	**5**	**1.98**	**4.1**				**6**	**2.89**	**3.6**		**0.89**
	10	**1**	**1.65**	**0.3**	**4**	**1.98**	**2.4**				**6**	**2.89**	**3.8**		**0.76**
	(*10*	*1*	*1.65*	*0.5*	*4*	*1.98*	*2.4*				*6*	*2.88*	*3.9*		*0.92*)[d]
	11	1	1.65	0.8	4	1.97	1.8	1	2.14	3	6	2.89	4.0		0.79
	12				5	1.98	4.1				6	2.89	4		1.46
	13				4	1.98	2.3				6	2.88	4.1		1.26
3a′	1				6	2.02	13							1.22	
	2				5	2.01	10							1.13	
	3				4	2.00	6.5							1.05	
	4				4	1.98	3.6	2	2.18	3				1.14	
	5	0.7	1.65	−1.0	5	2.00	8.5							0.72	
	6	0.7	1.65	0	3	1.97	2.1	2	2.13	5				0.52	
	7				6	2.02	13								1.40
	8				5	2.02	10								1.34
	9				4	1.98	3.2	2	2.17	2.1					1.29
	10	0.7	1.65	0.5	3	1.97	1.6	2	2.13	3					0.97
	11	**0.7**	**1.65**	**0.3**	**3**	**1.97**	**1.7**	**2**	**2.12**	**3.8**	**6**	**2.90**	**4.5**		**0.64**
	(*11*	*0.7*	*1.65*	*0.2*	*3*	*1.97*	*1.7*	*2*	*2.13*	*3.8*	*6*	*2.90*	*4.6*		*0.80*)[d]
	12				3	1.97	1.2	2	2.14	2.2	6	2.90	5		1.04
3b	1				6	1.99	2.6							1.58	
	2	1	1.68	0.3	5	1.98	1.7							0.81	
	3	1	1.67	1.3	4	1.98	0.4							0.66	
	4	1	1.67	1.5	4	1.98	0.4	1	2.19	15				0.69	
	5				6	1.99	2.7								1.67
	6	1	1.68	0.2	5	1.98	1.8								1.04
	7	**1**	**1.68**	**0.3**	**5**	**1.98**	**1.8**				**3**	**2.85**	**4**		**0.98**
	(*7*	*1*	*1.68*	*1.1*	*5*	*1.98*	*1.4*				*3*	*2.82*	*0.1*		*1.32*)[d]
	8	**1**	**1.68**	**0.2**	**5**	**1.98**	**1.8**				**4**	**2.86**	**6**		**0.98**
	9				5	1.98	1.5				3	2.81	3		1.43
3c	1				6	2.02	9							1.73	
	2				5	2.01	5.2							1.57	
	3	1	1.67	−0.9	5	2.00	5.2							0.94	
	4	1	1.67	−0.6	4	2.00	3.1							0.78	
	5	1	1.67	−0.4	4	2.00	2.6	1	2.21	3				0.68	
	6				6	2.02	9								1.85
	7				5	2.01	5.3								1.72
	8	1	1.67	−0.6	5	2.00	4.9								1.23
	9	1	1.67	−0.3	4	2.00	2.9								1.13
	10	1	1.67	0.2	4	2.00	1.9	1	2.18	−0.7					1.04
	11	**1**	**1.67**	**−0.6**	**5**	**2.00**	**4.8**				**6**	**2.91**	**4.7**		**1.03**
	12	**1**	**1.67**	**−0.5**	**4**	**2.00**	**2.9**				**6**	**2.91**	**4.9**		**0.84**
	(*12*	*1*	*1.67*	*0*	*4*	*1.99*	*2.6*				*6*	*2.90*	*5.0*		*1.15*)[d]
	13	1	1.67	0.2	4	1.99	1.9	1	2.18	−0.2	6	2.91	5.5		0.76
	14				4	2.00	2.7				6	2.90	5		1.47

[a] Fourier transformed range for **3a** and **3a′**: $k = 2-15$ Å^{-1}; for **3b** and **3c**: $k = 2-14.9$ Å^{-1} (resolution 0.12 Å). *r* is in units Å, $\Delta\sigma^2$ in 10^3 Å^2. Back-transformation range for **3a**: [b] $r' = 0.70-2.05$ Å; [c] $r' = 0.70-3.40$ Å; for **3a′**: [b] $r' = 0.75-2.05$ Å; [c] $r' = 0.75-3.25$ Å; for **3b**: [b] $r' = 0.60-2.10$ Å; [c] $r' = 0.60-3.05$ Å; for **3c**: [b] $r' = 0.70-2.10$ Å; [c] $r' = 0.70-3.20$ Å. [d] Fits to unfiltered data corresponding to the best fits to filtered data.

decay product is further corroborated by the EXAFS analysis on a sample of the pyO derivative **3a′** that contains 60% Fe^{IV} (by Mössbauer analysis). The fitting protocol for this sample also leads to a fit with four shells: 0.7 O/N at 1.65 Å ($\Delta\sigma^2$, 0.0003 Å^2), 3 N/O at 1.97 Å (0.0017), 2 N/O at 2.12 Å (0.0038), and 6 C at 2.90 Å (0.0045) (Table 4, fit 11, and Figure S7). The 2.12-Å shell may be attributed to the Fe−N distance of high-spin Fe^{III} byproducts that make up ca. 40% of the sample.

The EXAFS spectra of the oxoiron(IV) complexes of the pentadentate ligands N4Py and Bn-TPEN, **3b** and **3c**, can be simulated best by using three shells. They differ slightly in the coordination numbers *n* of the multi-nitrogen shell near 2.0 Å and of the multi-carbon shell near 2.9 Å, depending on the nature of the N-donor ligand. As observed for **2b**, the *n* value of the 2.0-Å shell in **3b** is 5, reflecting a narrow range of Fe−N distances, but the *n* value of the carbon shell is low, reflecting

(64) Chance, B.; Powers, L.; Ching, Y.; Poulos, T.; Schonbaum, G. R.; Yamazaki, I.; Paul, K. G. *Arch. Biochem. Biophys.* **1984**, *235*, 596−611.
(65) Green, M. T.; Dawson, J. H.; Gray, H. B. *Science* **2004**, *304*, 1653−1656.
(66) Consistent with the Mössbauer quantification, the short-distance shell could also be refined with an occupancy of $n < 1$ (Table S7).

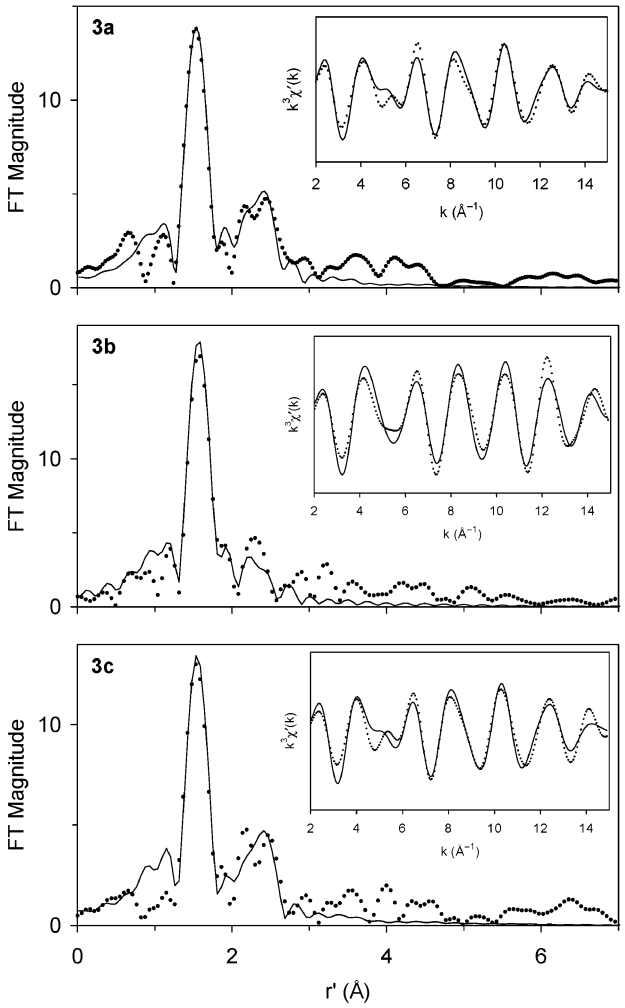

Figure 5. Fourier transforms of the Fe K-edge EXAFS data ($k^3\chi(k)$) and Fourier-filtered EXAFS spectra ($k^3\chi'(k)$, inset) of $[Fe^{IV}(O)(TPA)(solv)]^{2+}$, **3a**, Fourier transformed range $k = 2-15$ Å^{-1}; experimental data (···) and fit 1 O/N, 4 N/O, 6 C (—); Back-transformation range: $r' = 0.70-3.40$ Å (top); $[Fe^{IV}(O)(N4Py)]^{2+}$, **3b**, Fourier transformed range $k = 2-14.9$ Å^{-1}; experimental data (···) and fit 1 O/N, 5 N/O, 3 C (—); Back-transformation range: $r' = 0.60-3.05$ Å (middle); and $[Fe^{IV}(O)(Bn\text{-}TPEN)]^{2+}$, **3c**, Fourier transformed range $k = 2-14.9$ Å^{-1}; experimental data (···) and fit 1 O/N, 4 N/O, 6 C (—); Back-transformation range: $r' = 0.70-3.20$ Å (bottom).

a wide range of Fe···C distances: 1 O/N at 1.68 Å ($\Delta\sigma^2$, 0.0003 Å^2), 5 N/O at 1.98 Å (0.0018), and 3 C at 2.85 Å (0.004) (Table 4, fit 7, and Figure 5). On the other hand, **3c** has parameters similar to **3a**: 1 O/N at 1.67 Å ($\Delta\sigma^2$, −0.0005 Å^2), 4 N/O at 2.00 Å (0.0029), and 6 C at 2.91 Å (0.0049) (Table 4, fit 12, and Figure 5).

Discussion

We have analyzed the X-ray absorption spectra of two alkylperoxoiron(III) and four oxoiron(IV) complexes in order to obtain structural information on these thermally labile species. These complexes have been generated as intermediates in the reactions of iron(II) precursors with peroxides, representing the first examples of such species to be observed. With the exception of **3a**, for which a preliminary analysis has been reported,[26] this study presents the first structural information available on this series of novel intermediates. This systematic analysis enables us to establish the signatures of $Fe^{III}-OO^tBu$ and $Fe^{IV}=O$ groups.

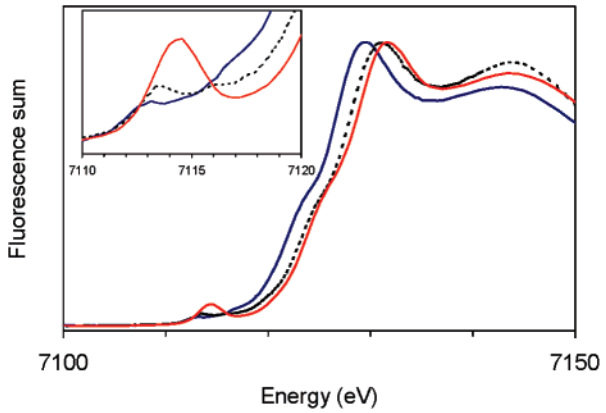

Figure 6. Fe K-edge X-ray absorption near-edge structures (XANES, fluorescence excitation) of $[Fe^{II}(N4Py)(NCMe)]^{2+}$, **1b** (blue —), $[Fe^{III}(N4Py)(OO^tBu)]^{2+}$, **2b** (- - -), and $[Fe^{IV}(O)(N4Py)]^{2+}$, **3b** (red —).

I. Information from XANES. Comparison of iron complexes of the same oxidation state with different supporting ligands shows that the Fe K-edge XANES features vary with the functionality, $Fe^{III}-OO^tBu$ or $Fe^{IV}=O$, as well as with the ligand environment of the absorbing atom (Figure 3). For the alkylperoxo complexes **2a** and **2b**, the K edges are found in a narrow window upshifted from that of **1b**, as expected for their higher oxidation state. Their preedge regions exhibit two peaks at 7113.5(1) and 7116.0(1) eV, associated with low-spin iron(III) centers,[51] with a total peak area of about 9−15 units, indicative of a metal center with a significant distortion from centrosymmetry.

The $Fe^{IV}=O$ series on the other hand exhibits a somewhat larger variability. The K edges of the two TPA complexes **3a** and **3a′** clearly show a further 1−1.5 eV increment relative to the alkylperoxo complexes, as may be expected for the increase in oxidation state, but those of the two N5 complexes **3b** and **3c** are just upshifted by less than 0.5 eV. These smaller changes may arise from the greater covalency of the iron(IV)-ligand bonds, particularly that of the Fe=O unit.[55] Unlike the alkylperoxo complexes, the iron(IV) complexes exhibit only one preedge feature, which is upshifted by about 0.6−1.1 eV with respect to the iron(III) complexes and has an intensity of 25−29 units.

Our systematic study provides an unprecedented opportunity to compare the XANES features of complexes of the same supporting ligand in three different oxidation states, all with low-spin configurations. As illustrated by the series of N4Py complexes **1b**, **2b**, and **3b** in Figure 6, the Fe K edges have very similar shapes and the edge shifts by less than 2 eV with an increase of the iron oxidation state from +II to +IV: $Fe^{II}-NCMe$, $Fe^{III}-OO^tBu$, $Fe^{IV}=O$. More striking is the progressive increase in the preedge peak area, from 4 units for **1b** to 15 units for **2b** and finally to 25 units for **3b**. This trend reflects the increased distortion from centrosymmetry as the MeCN ligand in the highly symmetric FeN_6 core in **1b** is progressively replaced with an alkylperoxo ligand in **2b** with a 1.78 Å Fe−O bond and then with the oxo ligand in **3b** with a 1.68 Å Fe−O bond.

II. Information from EXAFS−Metrical Trends. The first coordination spheres of the alkylperoxoiron(III) and oxoiron(IV) complexes discussed here can generally be described by two shells of metal−ligand scattering interactions: a longer

Table 5. Summary of EXAFS Fitting Results for the Iron Complexes in This Study

	Fe–N/O			Fe–N/O			Fe–N/O			Fe···C		
complex	*n*	*r* (Å)	$\Delta\sigma^2$	*n*	*r* (Å)	$\Delta\sigma^2$	*n*	*r* (Å)	$\Delta\sigma^2$	*n*	*r* (Å)	$\Delta\sigma^2$
iron(II)												
1b				5	1.96	3.6				3	2.82	4
alkylperoxoiron(III)												
2a	1	1.78	2.9	4	1.96	2.3				6	2.84	3.5
2b	1	1.78	0.4	5	1.97	1.5				3	2.82	6
oxoiron(IV)												
3a	1	1.65	0.3	4	1.98	2.4				6	2.89	3.8
3a′	0.7	1.65	0.3	3	1.97	1.7	2	2.12	3.8	6	2.90	4.5
3b	1	1.68	0.3	5	1.98	1.8				3	2.85	4
3c	1	1.67	−0.5	4	2.00	2.9				6	2.91	4.9

Table 6. Structural Parameters of Synthetic High-valent Fe=O Complexes[a]

complex	Fe–N	Fe–O	method	ref.
non-porphyrin				
$K_2[Fe^{VI}O_4]$		1.660−1.671	XRD	69
$Na_4[Fe^{IV}O_4]$[b]		1.790−1.825	XRD	70
$[Fe^{IV}(O)(TMC)(NCMe)](OTf)_2$[c]	2.058−2.117	1.646	XRD	25
porphyrin				
$[Fe^{IV}(O)(TMP)^{+\bullet}(MeOH)]^+$[d]	2.02	1.63−1.66	XAS	63
$[Fe^{IV}(O)(TMP)^{+\bullet}(X)]$, X = Cl, Br[d]	1.99, 2.01	1.66, 1.65	XAS	53
$[Fe^{IV}(O)(F_8TPP)^{+\bullet}]^+$[e]	2.00	1.67	XAS	54
$[Fe^{IV}(O)(TTP)(Me\text{-}im)]$[f]	2.03	1.65−1.66	XAS	63

[a] Distances are in Å. [b]powder diffraction. [c]TMC, 1,4,8,11-tetramethyl-1,4,8,11-tetraazacyclotetradecane. [d]TMP, *meso*-tetramesitylporphinato dianion. [e]F_8TPP, *meso*-tetrakis(2,6-difluorophenyl)porphinato dianion. [f]TTP, *meso*-tetra-*m*-tolylporphinato dianion; Me-im, *N*-methylimidazole. There is a crystal structure of an Fe^{IV}(O)(porphyrin) complex with an Fe−O bond length of 1.604 Å that was briefly mentioned in a footnote of Schappacher et al.,[71] but this result has not been subsequently presented in greater detail.

distance that accounts for 4−5 nitrogen atoms of the supporting ligand, and a shorter distance that arises from only 1 nitrogen/oxygen atom. The longer Fe−N distances fall within a very narrow range of 1.96−2.00 Å for the $S = 1/2$ Fe^{III} and $S = 1$ Fe^{IV} complexes, consistent with their low-spin nature (Table 5). In the series of N4Py complexes, **1b**, **2b**, and **3b**, the 2.0-Å shell remains nearly unchanged with the increase in oxidation state from +II to +IV; furthermore the 5-atom shell is consistently fit with a low Debye−Waller factor, reflecting the small range of Fe−N bond lengths. In contrast, there appears to be a greater variability of Fe−N bond lengths for the TPA and Bn-TPEN complexes that leads to some destructive interference, as the coordination numbers for the main shell in the best fits consistently have a value of 4. Nevertheless, the average Fe−N distance remains near 2 Å for these complexes.

Complexes **3a**, **3a′**, **3b**, and **3c** all have single scatterers with short Fe−O distances in the range of 1.65−1.68 Å, which are assigned to the Fe^{IV}=O group (Table 5). These distances closely match that found in the crystallographically characterized $[Fe^{IV}(O)(TMC)(NCMe)](OTf)_2$ (1.646(3) Å).[25] Furthermore, it agrees well with the corresponding distances in synthetic oxoiron(IV) porphyrins[53,54,62,63] (Table 6) and horseradish peroxidase Compounds I and II[62−65] determined by EXAFS analysis. The nonheme complexes reported here significantly augment the structural database for oxoiron(IV) complexes and demonstrate that the Fe=O distance of the $S = 1$ oxoiron(IV) unit is rather insensitive to the nature of the other ligands in the iron coordination sphere, be they neutral and pentadentate as in the case of N4Py or Bn-TPEN or dianionic and planar tetradentate as in the case of porphyrins. The consistently short Fe−O distance found for oxoiron(IV) complexes support DFT calculations that invariably describe the Fe^{IV}=O bond as a highly covalent interaction between the oxo atom and the $3d_{z2}$, $3d_{xz}$, and $3d_{yz}$ orbitals of the iron.[55,67,68]

Additional shells are needed to fit the EXAFS features observed under 3 Å for **3a**, **3a′**, **3b**, and **3c**. Common to all four complexes is a shell of low-*Z* atoms at 2.9 Å that are assigned to the carbon atoms adjacent to the ligating nitrogen atoms. Scrutiny of the fit protocols in Table 4 reveals that the addition of this shell makes a more marked improvement in the GOF value for TPA and Bn-TPEN complexes than for the N4Py complex. This difference may be due to the larger spread of Fe···C distances near 2.9 Å associated with N4Py, as found in the crystal structures of **1b** and $[Fe^{III}(N4Py)(OMe)]^{2+}$,[30] resulting in some destructive interference among the contributions to this shell.

The alkylperoxo intermediates **2a** and **2b** can, like the oxoiron(IV) complexes, be fit with three shells of scatterers. Besides the 2.0 Å principal shell that arises from the Fe−N bonds of the polydentate ligand, there is a single-scatterer shell at 1.78 Å assigned to the peroxo ligand and a multiscatterer shell at 2.8 Å due to the carbon atoms adjacent to the ligating N atoms. The single low-*Z* scatterer at 1.78 Å can be assigned to the Fe^{III}−OO^tBu bond, in agreement with DFT calculations on $[Fe^{III}(TPA)(OO^tBu)(OH_2)]^{2+}$.[22] This distance is comparable to the 1.76 Å Fe^{III}−OOH distance found for low-spin $[Fe^{III}(N4Py)(OOH)]^{2+}$ by EXAFS analysis[19] but is shorter than those found for low-spin Fe^{III}−OOH complexes with pentadentate ligands having one anionic group, $[Fe^{III}(S^{Me2}N_4(tren))(OOH)]^+$ (1.86 Å)[17] and $[Fe^{III}(PaPy3)(OOH)]^+$ (∼1.97 Å).[20] The additional anionic functionality in the latter two complexes probably competes with the peroxide ligand for the lone t_{2g} orbital on the low-spin iron(III) center available for π bonding.[72] Thus, unlike the oxo group in complexes **3**, the Fe^{III}−O distances of the peroxo ligands appear to be strongly modulated by the nature of the other ligands in the metal coordination sphere.

The binding mode of the alkylperoxo ligand deserves some comment. Most crystal structures of synthetic alkylperoxo complexes of 3d transition metals (e.g., Ti^{IV} (d^0), Mn^{II} (d^5), Co^{II} (d^7), Co^{III} (d^6), Cu^{II} (d^9)) have revealed end-on binding of the alkylperoxo group with M-OOR distances in the range 1.82−1.96 Å and M−O−O angles of 105−122°, with the distal oxygen atom of the M−OOR fragment found at distances of 2.68−2.95 Å from the metal center (Table 7). On the other hand, side-on binding can be observed with two complexes of $3d^0$ metal ions, Ti^{IV} and V^V, giving rise to M−OOR distances of 1.913 and 1.872 Å and M···OR distances of 2.269 and 1.999 Å, respectively (Table 7). We have considered whether our data allow us to distinguish between the two binding modes for **2a** and **2b**. The observed 1.78-Å distances and the fact that **2a** and **2b** are both low-spin complexes would certainly favor an end-

(67) Zhang, Y.; Oldfield, E. *J. Am. Chem. Soc.* **2004**, *126*, 4470−4471.
(68) Ghosh, A.; Almlöf, J.; Que, L., Jr. *J. Phys. Chem.* **1994**, *98*, 5576−5579.
(69) Hopper, M. L.; Schlemper, E. O.; Murmann, R. K. *Acta Crystallogr.* **1982**, *B38*, 2237−2239.
(70) Weller, M. T.; Hector, A. L. *Angew. Chem., Int. Ed.* **2000**, *39*, 4162−4163.
(71) Schappacher, M.; Weiss, R.; Montiel-Montoya, R.; Trautwein, A.; Tabard, A. *J. Am. Chem. Soc.* **1985**, *107*, 3736−3738.
(72) Neese, F.; Zaleski, J. M.; Zaleski, K. L.; Solomon, E. I. *J. Am. Chem. Soc.* **2000**, *122*, 11703−11724.

Table 7. Structural Parameters of Fe(OOH), Fe(η^2-O_2), and Fe(OOR) Complexes and M(OOR) Complexes of Other 3d Metals (nonbridging peroxo ligands)[a]

complex	spin state	M–N[b]	M–O	M···O	method	ref.
		end-on peroxo complexes of Fe				
$[Fe^{III}(S^{Me2}N_4(tren))(OOH)]^{+}$ [c]	low spin	2.01	1.86	2.78	XAS	17
$[Fe^{III}(N4Py)(OOH)]^{2+}$ [d]	low spin	1.96	1.76		XAS	19
$[Fe^{III}(qn)_2(OOC(O)O)]^{-}$ [e]	high spin	2.182	1.936	2.871	XRD	73
purple lipoxygenase (1IK3.pdb; 2.0 Å resolution)[f]	high spin	2.2−2.3	2.0	2.8	XRD	10
		side-on peroxo complexes of Fe				
$[Fe^{III}(N4Py)(\eta^2\text{-}O_2)]^{+}$ [d]	high spin	2.20	1.93		XAS	19
NDO:indole:dioxygen (1O7N.pdb; 1.4 Å resolution)[g]		2.1−2.2	1.8	2.0	XRD	14
		end-on alkylperoxo complexes of other 3d metals				
$[Ti^{IV}ClCp_2(OO^tBu)]$			1.909	2.952	XRD	74
$[Mn^{II}(Tp^{tBu,iPr})(OOCMe_2Ph)]$ [h]	high spin	2.132−2.161	1.964	2.700	XRD	75
$[Co^{II}(Tp^{tBu,iPr})(OOCMe_2Ph)]$ [h]	high spin	2.01−2.06	1.86	2.71	XRD	76
$[Cu^{II}(Tp^{iPr,iPr})(OOCMe_2Ph)]$ [h]		1.949−2.161	1.816	2.737	XRD	77
$[Co^{III}(L)(OOR)]$ [i]	low spin	1.917−2.024	1.838	2.683	XRD	*i*
			−1.905	−2.826		
		side-on alkylperoxo complexes of other 3d metals				
$\{[Ti^{IV}(tea)(\eta^2\text{-}O_2{}^tBu)]\}_2$ [j]		2.299	1.913	2.269	XRD	78
$[V^{V}(L)(O)(\eta^2\text{-}O_2{}^tBu)(OH_2)]$ [k]			1.872	1.999	XRD	79

[a] Distances are in Å; average values are reported for crystallographic disorder and independent molecules. [b] M−N distance of amine, imidazole, and pendant pyridine groups. [c] $HS^{Me2}N_4$(tren), 3-[*N*-[2-[*N*,*N*-bis(2-aminoethyl)amino]ethyl]imino]-2-methyl-2-butanethiol. [d] N4Py, *N*,*N*-bis(2-pyridylmethyl)-*N*-bis(2-pyridyl)methylamine. [e] Hqn, 2-quinolinecarboxylic acid. [f] Purple lipoxygenase, from soybean lipoxygenase-3 and (9*Z*,11*E*)-13(*S*)-hydroperoxy-9,11-octadecadienoic acid. [g] NDO, naphthalene dioxygenase from *Pseudomonas* sp. [h] $Tp^{tBu,iPr}$, hydrotris(3-*tert*-butyl-5-isopropylpyrazol-1-yl)borate; $Tp^{iPr,iPr}$, hydrotris(3,5-diisopropylpyrazol-1-yl)borate. [i] Selected examples: $[Co^{III}(acac)_2(OO^tBu)(L)]$, L = py, Me-im;[80] $[Co^{III}(dbm)_2(OO^tBu)(py)]$;[80] $[Co^{III}(Py_3P)(OOR)]$, R = ^{t}Bu, CMe_2Ph, CMe_2Bn;[81,82] $[Co^{III}(BPI)(OO^tBu)(OBz)]$;[83] $[Co^{III}(Hdmg)_2(OOCMe_2Ph)(py)]$;[84] $[Co^{III}(tren)(OOCHMeCO_2)]^{+}$;[85] abbreviations: Hacac, 2,5-pentanedione; Me-im, *N*-methylimidazole; Hdbm, 1,3-diphenyl-1,3-propanedione; Py_3PH_2, *N*,*N*-bis[2-(2-pyridyl)ethyl]pyridine-2,6-dicarboxamide; BzOH, benzoic acid; BPI = 1,3-bis(2′-pyridylimino)isoindoline; H_2dmg, 2,3-butanedione dioxime; tren, tris(2-aminoethyl)amine. [j] H_3tea, 2,2′,2″-nitrilotriethanol. [k] H_2L = 2,6-pyridinedicarboxylic acid.

on binding mode. In such a binding mode, the distal oxygen atom would be expected to be 2.7−3.0 Å from the metal center. It would thus be included with the scatterers in the 2.8-Å multicarbon shell from the TPA and N4Py ligand backbones, unlike in the case of $[Fe^{III}(S^{Me2}N_4(tren))(OOH)]^{+}$, where the lack of such a carbon shell allows an oxygen scatterer at 2.78 Å to be discerned in the EXAFS analysis.[17] On the other hand, a side-on bound alkylperoxide would be expected to introduce an additional oxygen scatterer in the range of 2.0−2.3 Å. Such an additional shell is not required in the analyses. It is also possible that the distal oxygen could have a short enough Fe−O distance to be part of the principal sub-shell at 2 Å. If one compares different intermediates with the same ligand, e. g. **2a** and **3a** (TPA) or **2b** and **3b** (N4Py), the coordination number for either the 2.0 or 2.8 Å shell remains constant with little change in the Debye−Waller factor (Table 5), suggesting the same number of scatterers in the two pairs of intermediates in the same series. The strongest argument against a side-on peroxo binding mode for **2a** and **2b** is the fact that such complexes are to date all high-spin, even in the case of porphyrins. Thus, we favor end-on coordination of the alkylperoxo group in **2a** and **2b**.

Perspective

We have used X-ray absorption spectroscopy to gain structural insight into thermally labile low-spin alkylperoxoiron(III) and oxoiron(IV) complexes that model possible intermediates in the dioxygen activation cycles of nonheme iron enzymes. Except for the crystallographically characterized $[Fe^{IV}(O)(TMC)(NCMe)]^{2+}$,[25] the data reported here constitute the only collection of metrical data available for these novel intermediates. These results serve as benchmarks with which to compare data on new enzyme intermediates.

To date, only one oxoiron(IV) intermediate has been identified for a mononuclear nonheme iron oxygenase.[11−13] Very recent EXAFS data on such an intermediate derived from TauD (taurine:2-oxoglutarate dioxygenase) revealed a 1.62 Å Fe−O bond,[86] comparable in length to those found for the synthetic oxoiron(IV) complexes reported here. Mössbauer analysis however determined the iron(IV) center in this species to be high spin,[11,86] as opposed to low spin for the synthetic complexes. Despite the difference in spin states, the comparable bond lengths are consistent with DFT calculations on the oxoiron(IV) unit and can be rationalized by the fact that the d_{xy} and the d_{x2-y2} orbitals, which are the orbitals affected by the spin state change, are not involved in Fe=O bonding interactions.[55]

(73) Hashimoto, K.; Nagatomo, S.; Fujinami, S.; Furutachi, H.; Ogo, S.; Suzuki, M.; Uehara, A.; Maeda, Y.; Watanabe, Y.; Kitagawa, T. *Angew. Chem., Int. Ed.* **2002**, *41*, 1202−1205.
(74) DiPasquale, A. G.; Kaminsky, W.; Mayer, J. M. *J. Am. Chem. Soc.* **2002**, *124*, 14534−14535.
(75) Komatsuzaki, H.; Sakamoto, N.; Satoh, M.; Hikichi, S.; Akita, M.; Moro-oka, Y. *Inorg. Chem.* **1998**, *37*, 6554−6555.
(76) Hikichi, S.; Komatsuzaki, H.; Akita, M.; Moro-oka, Y. *J. Am. Chem. Soc.* **1998**, *120*, 4699−4710.
(77) Kitajima, N.; Katayama, T.; Fujisawa, K.; Iwata, Y.; Moro-oka, Y. *J. Am. Chem. Soc.* **1993**, *115*, 7872−7873.
(78) Boche, G.; Möbus, K.; Harms, K.; Marsch, M. *J. Am. Chem. Soc.* **1996**, *118*, 2770−2771.
(79) Mimoun, H.; Chaumette, P.; Mignard, M.; Saussine, L.; Fischer, J.; Weiss, R. *Nouv. J. Chim.* **1983**, *7*, 467−475.
(80) Chavez, F. A.; Briones, J. A.; Olmstead, M. M.; Mascharak, P. K. *Inorg. Chem.* **1999**, *38*, 1603−1608.
(81) Chavez, F. A.; Nguyen, C. V.; Olmstead, M. M.; Mascharak, P. K. *Inorg. Chem.* **1996**, *35*, 6282−6291.
(82) Chavez, F. A.; Rowland, J. M.; Olmstead, M. M.; Mascharak, P. K. *J. Am. Chem. Soc.* **1998**, *120*, 9015−9027.
(83) Saussine, L.; Brazi, E.; Robine, A.; Mimoun, H.; Fischer, J.; Weiss, R. *J. Am. Chem. Soc.* **1985**, *107*, 3534−3540.
(84) Giannotti, C.; Fontaine, C.; Chiaroni, A.; Riche, C. *J. Organomet. Chem.* **1976**, *113*, 57−65.
(85) Kojima, M.; Akhter, F.; Nakajima, K.; Yoshikawa, Y. *Bull. Chem. Soc. Jpn.* **1996**, *69*, 2889−2895.
(86) Riggs-Gelasco, P. J.; Price, J. C.; Guyer, R. B.; Brehm, J. H.; Barr, E. W.; Bollinger, J. M., Jr.; Krebs, C. *J. Am. Chem. Soc.* **2004**, *126*, 8108−8109.

Thus an obvious target for future synthetic efforts is the generation and characterization of a high-spin oxoiron(IV) complex.

An EXAFS analysis of chloroperoxidase Compound II has also been recently reported.[65] In this case, the Fe−O distance was determined to be 1.82 Å, significantly longer than those found for horseradish peroxidase Compound II and the synthetic complexes described in this paper. This lengthening has been ascribed to the protonation of the oxoiron(IV) unit, a phenomenon also observed for other,[87−89] but not all,[63,65] Compounds II. The oxoiron(IV) centers in peroxidase Compounds II may be expected to be more prone to protonation because the dianionic porphinate should diminish the Lewis acidity of the metal center; for chloroperoxidase, the additional thiolate ligand further enhances this effect. On the other hand, the oxoiron(IV) centers of complexes **3** have neutral ligands, making the metal center significantly more Lewis acidic and the oxo group more difficult to protonate. The availability of well characterized oxoiron(IV) complexes with a range of supporting ligands thus provides us with a better basis for understanding the fundamental properties of these novel high-valent species.

(87) Berglund, G. I.; Carlsson, G. H.; Smith, A. T.; Szöke, H.; Henriksen, A.; Hajdu, J. *Nature* **2002**, *417*, 463−468.
(88) Bonagura, C. A.; Bhaskar, B.; Shimizu, H.; Li, H.; Sundaramoorthy, M.; McRee, D. E.; Goodin, D. B.; Poulos, T. L. *Biochemistry* **2003**, *42*, 5600−5608.
(89) Hersleth, H.-P.; Dalhus, B.; Görbitz, C. H.; Andersson, K. K. *J. Biol. Inorg. Chem.* **2002**, *7*, 299−304.

Acknowledgment. This work was supported by grants from the National Institutes of Health (GM-33162 to L.Q.) and the Ministry of Science and Technology of Korea through the Creative Research Initiative Program (to W.N.) and a fellowship from the Deutsche Forschungsgemeinschaft (to J.-U.R.). We are grateful to Audria Stubna and Prof. Eckard Münck of the Carnegie Mellon University for Mössbauer analyses of the XAS samples. We thank Dr. Neil R. Brooks of the University of Minnesota X-ray Crystallographic Facility for the crystal structure determination of **1b**$(OTf)_2$. XAS data were collected on beamline 7-3 at the Stanford Synchrotron Radiation Laboratory and beamline X9B at the National Synchrotron Light Source, both supported by the US Department of Energy and the National Institutes of Health. We thank Dr. Matthew J. Latimer at SSRL and Dr. Nebojsa S. Marinkovic at NSLS for their excellent technical support of our synchrotron experiments.

Supporting Information Available: Fe K-edge EXAFS spectra of all compounds (Figures S1 and S2) and detailed EXAFS fitting protocols (Tables S2−S10). Best fits (Fourier transforms of Fe K-edge EXAFS data and Fourier-filtered EXAFS spectra) for **1b**, duplicate **2a**, and **3a′** (Figures S4−S7, PDF). Details of the crystal structure determinations of **1b**$(OTf)_2$ and **1c**(OTf) (Tables S1, S11, S12, and Figure S9, PDF) and X-ray crystallographic files (CIF). This material is available free of charge via the Internet at http://pubs.acs.org.

JA047667W